ISSN No:-2456-2165

White Hole Observation: An Experimental Result

Yang Immanuel Pachankis
Building 2 Dexin Yuan, 1001 Biqing N Rd,
Chongqing, 402762, PRC

Abstract:- The article presents the empirical confirmation to the black hole and white hole juxtapose theory. The author based the experiment on the multi-mission multi-spectral space telescope data conducted remotely with the NASA Data Challenge and Harvard-Smithsonian Micro-Observatory. Since the loss of the original manuscript, the author reformulated the mathematics during the research. The observation developed a resonance observation technique that observed the white hole to the moon's direction with the sun. The data reduction of the white hole and other observations provides an explanation for the undetected gravitons and some empirical physical features of the white hole.

Keywords:- *gravitational singularities; interdisciplinary astronomy; astronomy data reduction; theoretical techniques; white hole; singularities; resonance observation; anti-entropy; space astrometry.*

I. INTRODUCTION

Baryon-rich, dark-matter-deficient dwarf galaxies at high redshift from the mass swept out in the intergalactic medium by energetic outflows from luminous quasars were predicted in 1999.[13] The representative samples of the baryonic rich low surface brightness galaxies embedded in dark matter halos of lower density and more extended than the halos around high surface brightness (HSB) disk galaxies were predicted to influence massive star formation, and no stars at all should form in low surface brightness (LSB) disks.[8] The experimental observation has produced evidence for the very few LSB galaxies with nuclear activity with temperatures below absolute zero with the sample of the M20 Trifid Nebula (*Figure 9 - 11*). The Virgo constellation with the black hole (BH) in M87 was among the first being detected in the experimental observation series with the both space and time like singularity shown in *Figure 18* with the observation data described in *Table 1*.The Southern Pinwheel observation approached the BH-white hole (WH) theory with galactic nuclei observation shown in *Figure 15*. Among the different approaches in direct observation on the WH, the moon observation begot the most direct observation on the WH shown in *Figure 1* with scalar boson field background. Apart from the shock-waves from the gravitational well shown in *Figure 2* that may have contributed to the occultation on the BH-WH juxtapose in the Hubble optical scheme, the ejected dark matter crystals may have caused further flares in all wavelength bands. This provides a basis for reading the WH observation on M87 shown in *Figure 20*, and the radiation light cone on the Southern Pinwheel shown in *Figure 17*. For observation it is generally assumed that BH does not emit light information as shown in *Figure 15* and *Figure 18*, but the later works of Stephen Hawking's suggested otherwise with the soft-hair theorem which the author also noticed in the Chandra X-ray histogram on NGC 3034.[9] [15] The author based the observation in parallel to the merged luminosity reference frame on NGC 3034 shown in *Figure 6* with an anti-entropy rationale for the ground-based observatory observation using the merged reference frame of the weak force slit shown in *Figure 8*. With the deduction to the key on the original theory, the author proposes an alternative understanding of light based on Lorentz transformation's application to particle physics for further empirical analysis on the WH data.

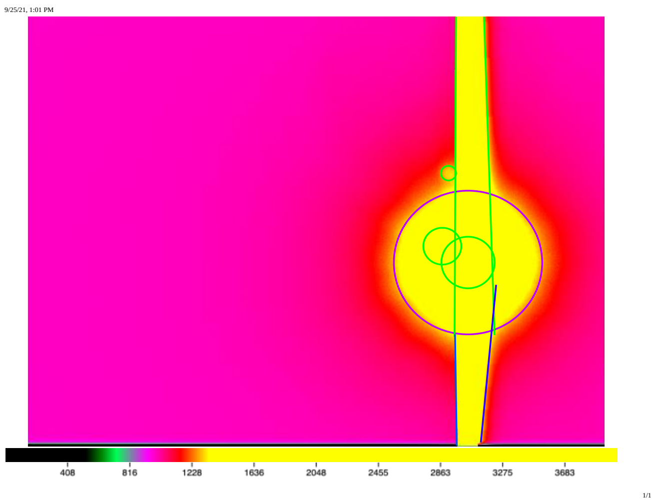

Fig. 1: Direct observation on the gravity curved space and the source of spatial curvature.

The observation used quantum data approach with Einsteinium gravity and the construct of the observation forms a resonance technique. Quantum spins are not counted in the research and observation, but in theory can provide a numerical value to the probable times of a BH hitting the critical mass as implied in Ruth A. Daly's approach in BH physics. Daly's team's approach in dark energy accounting for cosmology has an empirical reference to the determination of the Big Bang theory with quantitative BH population. The observational work serves as constructive research to a possible model on the probable times of the Big Bang the universe have experienced to the formation of the observed system today, as differentiated from the time of human civilization or planetary development such as the earth.[4] Answering this question may provide further insights into the cosmic censorship.[8] The observational results, with rare cases of LSB to a linear HSB at the probable WH sample do not assume fragmented gravitational collapse.[12][8] Even though the momentary velocity of the detection was compromised by distance and restricted to the photon appearances, the scale of the galactic bulge's direct contribution to the solar wind and its LSB characteristics with intense beam suggests on the linear WH observation due to the nuclear resonance effect and the tidal lock.

ISSN No:-2456-2165

Neutrinoless double beta decay under experiment by Yale University may provide further insight into quantum gravity as suggested in the observation in *Figure 13*, but in observational astronomy the fissile chains and possible exotic matters shown in *Figure 11* & *Figure 12* are still the limitations to furtherinsights into the interior regions. As an alternative, the dark star postulate has put the quantum indeterminacy and spatial depth on the same footing and provides a possible link between solid state physics research and instrumentation for astrochemistry.[1]

It was for the theoretical background, the observation adopted multi-spectral analysis on the space telescope data, and did not follow the Hubble optical schemes. The strong force was inducted from the Chandra X-ray space telescope data before the observation, and the material fields of the WH on NGC 3034 with the Kerr-Newman (KN) case was processed after the observation shown in *Figure 5*. The author reformulated the mathematics of the original theory during the data research. The singularities were described in a dynamic geometry instead of seeking a concrete form of answer in algebra. In this sense, information and the light speed of information have replaced the traditional Einsteinium concept of light with the aid of sky-grip in the JS9-4L system provided at the backend. This allowed the Einstein field equation being adopted in direct reading on the local universe. As it was pointed out, deviations from spherical symmetry cannot prevent space-time singularities from arising and actual physical singularities are not permitted to occur, the author approached this dilemma with that fusion and fission can be simultaneously occurring in the internal regions of BH.[18] It is therefore, the KN case on NGC 3034 is the best and easiest model to derive the mathematics with practical limitations in instrumentation. The use of *i* in the notation gives both a flexibility in the times of critical mass have experienced in the local BH-WH juxtapose, and possible meanings in particle physics such as the deep electron orbit theory.[11] The Hamiltonian zero $\vec{0}$ is introduced for the empirical discretion on the infinities involved in the celestial phenomenon along with the binomial result in *Theorem 6* for further anti-entropy methodological developments. The empirical particle physics required for the determination of critical mass terms in the cosmic abundance of matter will need further laboratory experiments. It is in this regard, the observational results, in the reverse order of the writing:

- captured the plasma high curvature on a two-dimensional imaging plate,
- does not violate Einstein's equation in spatial depth,
- shift the space-time manifold to instrumentation orbit,
- change local energy to terms of possible local chemistry.[18]

The particle physics perspective the author adopts is based on the probabilistic distribution on matters that may need to hit multiple times of critical mass to form. This in theory would provide insights to the Big Bang determinants and a probable model for cosmic space-time based on the solar matter distribution. The fundamentals of the juxtapose theory holds that the causality on the emergence of exotic matters is on the oscillation of BH and WH, and the categorization on the four types of BHs vary by local chemistry & thermal dynamics.[15] The observation did not quantify the critical mass of BHs nor an empirical determination for dark energy on the cosmological sense, and only aimed at using a different solar object to possibly reference the WH mass as the moon. Therefore, the observational result differed from Daly's team's by the key aspect in spatial curvature that is accounted for the cosmological expansion.[4] Albeit the experimental observation replaced the k determinant with κ for instrumentation rationale, the observational method only aimed at establishing the astronomical factual and physical existence of WH first which is supported by eternal black hole theories as the deduced data shown in *Figure 2*&*Figure 4*. [10][4]*Figure 9* provides with the best proof for the existence of WH in the observational results on M20, and the moon observation provides the most direct result of the WH observation.

In the observational data processing, for the basic functions of JS9-4L online, *Shift / Bias* adjusts the meridian of the telescope observation data, *Stretch / Contrast* adjusts the depth-of-view of the light information to the observer's corona as bits per pixel to the two-dimensional array, and the brightness limits adjusts the thresholdof data parameters to the astro-particle momenta with temperature in multi-spectral optics, which is to say the thermionic density of astro-particles in the observational images are adjusted by brightness limits. The scale panel adds trigonometric analysis to the data structure, and linear function is used to illustrate the forces involved in micro-observatory observation method. The robotic telescope network uses local sidereal time to track the observational exposures, and the temperature data is based on ambient telescope and CCD camera temperatures in Kelvin with relative humidity and weather indicators. The whole series of observations is principally organized by universal time with variations in Modified Julian Date (MJD) and local mean sidereal time (LST) at start of observation in J2000 epoch. LST is used as a parameter of space, and MJD is used as a parameter of time. For the structure of this article, the author's epistemic causal inference model is data driven from special relativity to instrumentation orbits as a supplement of general relativity.[5] The extensive group of experiment on M87 after the May 2021 sun observation is not going to be discussed in the article for it would require further detailed particle physics analysis that the author does not have the proper equipment for.

Table 1. Micro-Observatory Observations 2020 - 2021

	Time of Observation		Observation Spatial Parameters						
Observed Object	Universal Time		Geographic Coordinate		Spatial Direction			Altitude & Azimuth	
	Date	Time	Latitude θ	Longitude λ	RA	HA	DEC	α	γ
(1)	(2)	(3)	(4)	(5)	(6)	(7)	(8)	(9)	(10)
Small Magellanic Cloud	2020-10-26	02:18:14.502-0000	-30.17	70.80	15.107684	343.566679	-71.969435	+47.269	172.586
Southern Pinwheel	2020-12-02	07:33:26.830-0000	-30.17	70.80	204.532319	269.626743	-29.968250	+14.251	116.647
Dark-D Calibration	2020-12-02	03:00:33.419-0000	-30.17	70.80	45.000000	0.713843	-30.000000	+89.359	285.209

Digitization					Local Observation Time Parameters				
Image Scale	Pixel Depth	Matrix Dimension		Exposure Time	Local Mean Sidereal Time	Arrow of Time			
arcsec/pixel	bits/pixel	Width (bytes)	Number of Rows	seconds	24h	MJD	RA	HA	DEC
(11)	(12)	(13)	(14)	(15)	(16)	(17)	(18)	(19)	(20)
5.240	16	650	500	060.00	20:54:14	59148.096	01:00.43	22:54.27	-71:58.17
5.240	16	650	500	060.00	04:36:10	59185.315	13:38.13	17:58.51	-29:58.10
5.240	16	650	500	060.00	00:02:32	59185.125	03:00.00	00:02.86	-30:00.00

	Technical Parameters						
Local Time Elapsed	Filter	Camera Status	Main Camera Focus	CCD Temperature	Ambient Telescope Temperature	Relative Humidity	Clear Sky Conditions
Differences in UT				Kelvin	Kelvin	Percentage	0-100
(21)	(22)	(23)	(24)	(25)	(26)	(27)	(28)
00:01:04.163-0000	Clear	High	none	265.0	287.0	21	093
00:01:02.069-0000	Clear	Out	350	265.0	282.0	21	093
00:01:02.109-0000	Opaque	Out	350	266.0	284.0	23	100

NOTE—The two main technical modes of operation are main in ZOOM and finder in resolution with camera status. The main telescope tracking is sidereal except for solar objects with parameters for main camera center.

ISSN No:-2456-2165

Table 1. Micro-Observatory Observations 2020 - 2021

Observed Object	Time of Observation Universal Time Date	Time	Observation Spatial Parameters Geographic Coordinate Latitude θ	Longitude λ	Spatial Direction RA	HA	DEC	Altitude & Azimuth α	γ
(1)	(2)	(3)	(4)	(5)	(6)	(7)	(8)	(9)	(10)
Virgo A M87	2021-04-24	03:12:12.098-0000	42.38	71.13	187.965593	1.323897	12.284138	+59.882	182.579
Dark-A Calibration	2021-04-24	04:01:51.668-0000	42.38	71.13	195.000000	6.698372	40.000000	+84.428	246.960
Moon	2021-04-27	04:47:36.906-0000	-30.17	70.80	216.460162	0.035747	-11.107931	+70.938	359.893

Digitization Image Scale arcsec/pixel	Pixel Depth bits/pixel	Matrix Dimension Width (bytes)	Number of Rows	Exposure Time seconds	Local Observation Time Parameters Local Mean Sidereal Time 24h	Arrow of Time MJD	RA	HA	DEC
(11)	(12)	(13)	(14)	(15)	(16)	(17)	(18)	(19)	(20)
4.140	16	650	500	060.00	08:36:32	59328.133	12:31.86	00:05.30	+12:17.05
4.140	16	650	500	060.00	09:26:19	59328.168	13:00.00	00:26.79	+40:00.00
5.240	16	650	500	000.10	10:25:20	59331.200	14:25.84	00:00.14	-11:06.48

Local Time Elapsed Differences in UT	Technical Parameters Filter	Camera Status	Main Camera Focus	CCD Temperature Kelvin	Ambient Telescope Temperature Kelvin	Relative Humidity Percentage	Clear Sky Conditions 0-100
(21)	(22)	(23)	(24)	(25)	(26)	(27)	(28)
00:01:02.062-0000	Clear	Out	1300	013.0	286.0	17	094
00:01:02.108-0000	Opaque	Out	1300	023.0	285.0	17	094
00:00:02.289-0000	Grey (ND4)	High	none	265.0	284.0	30	096

Note—In the moon observation, I have received two pieces of data with the same parameters except for the reversal of image axis. The center of main camera in finder camera is 495, 218 with sidereal tracking. The Observation Start Date on M87 was $2021 - 04 - 23T23 : 12 : 12.098 - 0400$.

Table 1. Micro-Observatory Observations 2020 - 2021

Observed Object	Time of Observation Universal Time Date	Time	Observation Spatial Parameters Geographic Coordinate Latitude θ	Longitude λ	Spatial Direction RA	HA	DEC	Altitude & Azimuth α	γ
(1)	(2)	(3)	(4)	(5)	(6)	(7)	(8)	(9)	(10)
Dark-B Calibration	2021-04-27	07:00:32.606-0000	31.68	110.88	210.000000	359.702630	30.000000	+88.301	171.282
Trifid Nebula M20	2021-04-27	11:26:29.551-0000	31.68	110.88	270.893661	5.436725	-23.032440	+35.041	186.113
Trifid Nebula M20	2021-04-27	11:28:17.422-0000	31.68	110.88	270.893661	5.921382	-23.032440	+34.995	186.655

Digitization Image Scale arcsec/pixel	Pixel Depth bits/pixel	Matrix Dimension Width (bytes)	Number of Rows	Exposure Time seconds	Local Observation Time Parameters Local Mean Sidereal Time 24h	Arrow of Time MJD	RA	HA	DEC
(11)	(12)	(13)	(14)	(15)	(16)	(17)	(18)	(19)	(20)
5.180	16	650	500	060.00	06:57:49	59331.292	14:00.00	23:58.81	+30:00.00
5.180	16	650	500	060.00	11:24:30	59331.477	18:03.57	00:21.75	-23:01.95
5.180	16	650	500	060.00	11:26:18	59331.478	18:03.57	00:23.69	-23:01.95

Local Time Elapsed Differences in UT	Technical Parameters Filter	Camera Status	Main Camera Focus	CCD Temperature Kelvin	Ambient Telescope Temperature Kelvin	Relative Humidity Percentage	Clear Sky Conditions 0-100
(21)	(22)	(23)	(24)	(25)	(26)	(27)	(28)
00:01:02.103-0000	Opaque	Out	1850	277.0	288.0	-2	000
00:01:02.061-0000	Red	Out	1825	275.0	284.0	06	000
00:01:02.106-0000	Green	Out	1825	274.0	284.0	10	000

Note—The Bose-Einstein condensate observed in the M20 data pact may either be the cause of or influenced by the oddity in the technical parameters on humidity and sky condition, and the latter is less likely the case.

Table 1. Micro-Observatory Observations 2020 - 2021

Observed Object	Time of Observation Universal Time Date	Time	Observation Spatial Parameters Geographic Coordinate Latitude θ	Longitude λ	Spatial Direction RA	HA	DEC	Altitude & Azimuth α	γ
(1)	(2)	(3)	(4)	(5)	(6)	(7)	(8)	(9)	(10)
Trifid Nebula M20	2021-04-27	11:30:14.279-0000	31.68	110.88	270.893661	6.372614	-23.032440	+34.949	187.159
Sun	2021-05-06	15:59:52.997-0000	42.38	71.13	43.871435	349.671227	16.721270	+62.864	157.884
Virgo A M87	2021-08-04	01:37:44.457-0000	42.38	71.13	187.965593	78.182777	12.284138	+16.931	271.335

Digitization Image Scale arcsec/pixel	Pixel Depth bits/pixel	Matrix Dimension Width (bytes)	Number of Rows	Exposure Time seconds	Local Observation Time Parameters Local Mean Sidereal Time 24h	Arrow of Time MJD	RA	HA	DEC
(11)	(12)	(13)	(14)	(15)	(16)	(17)	(18)	(19)	(20)
5.180	16	650	500	060.00	11:28:15	59331.479	18:03.57	00:25.49	-23:01.95
5.160	16	650	500	000.25	22:13:36	59340.667	02:55.49	23:18.68	+16:43.28
4.140	16	650	500	060.00	13:43:57	59430.068	12:31.86	05:12.73	+12:17.05

Local Time Elapsed Differences in UT	Technical Parameters Filter	Camera Status	Main Camera Focus	CCD Temperature Kelvin	Ambient Telescope Temperature Kelvin	Relative Humidity Percentage	Clear Sky Conditions 0-100
(21)	(22)	(23)	(24)	(25)	(26)	(27)	(28)
00:01:02.102-0000	Blue	Out	1875	274.0	284.0	10	000
00:00:02.287-0000	Grey (ND4)	High	none	276.0	299.0	52	094
00:01:02.102-0000	Blue	Out	1350	000.0	299.0	38	000

Note—The sun observation used solar tracking with the center of main camera in finder camera on 377, 239. The M87 observation started at $2021 - 08 - 03T21 : 37 : 44.457 - 0400$ and belongs to an extensive experiment group.

Table 1. Micro-Observatory Observations 2020 - 2021

Observed Object	Time of Observation Universal Time Date	Time	Observation Spatial Parameters Geographic Coordinate Latitude θ	Longitude λ	Spatial Direction RA	HA	DEC	Altitude & Azimuth α	γ
(1)	(2)	(3)	(4)	(5)	(6)	(7)	(8)	(9)	(10)
Virgo A M87	2021-08-04	01:42:23.516-0000	42.38	71.13	187.965593	79.269077	12.284138	+16.129	272.060
Dark A Calibration	2021-08-04	04:00:24.143-0000	42.38	71.13	300.000000	1.866730	40.000000	+87.237	211.170

Digitization Image Scale arcsec/pixel	Pixel Depth bits/pixel	Matrix Dimension Width (bytes)	Number of Rows	Exposure Time seconds	Local Observation Time Parameters Local Mean Sidereal Time 24h	Arrow of Time MJD	RA	HA	DEC
(11)	(12)	(13)	(14)	(15)	(16)	(17)	(18)	(19)	(20)
4.140	16	650	500	060.00	13:48:36	59430.071	12:31.86	05:17.08	+12:17.05
4.140	16	650	500	060.00	16:07:00	59430.167	20:00.00	00:07.47	+40:00.00

Local Time Elapsed Differences in UT	Technical Parameters Filter	Camera Status	Main Camera Focus	CCD Temperature Kelvin	Ambient Telescope Temperature Kelvin	Relative Humidity Percentage	Clear Sky Conditions 0-100
(21)	(22)	(23)	(24)	(25)	(26)	(27)	(28)
00:01:02.104-0000	Red	Out	1350	001.0	300.0	18	000
00:01:02.108-0000	Opaque	Out	1350	000.0	300.0	18	000

Note—The series of M87 observation requested was designed to utilize RGB filters and dark calibration to manage the observation on white hole on the end phase of thermionic black hole accretion. The order of observation filters were reconstructed on the data feedback. It could be contributed to the factor of instrumentation security and thermionic capacity in data recording.

Table 1. Micro-Observatory Observations 2020 - 2021

Observed Object	Time of Observation Universal Time Date	Time	Observation Spatial Parameters Geographic Coordinate Latitude θ	Longitude λ	Spatial Direction RA	HA	DEC	Altitude & Azimuth α	γ
(1)	(2)	(3)	(4)	(5)	(6)	(7)	(8)	(9)	(10)
Virgo A M87	2021-08-04	01:37:44.457-0000	42.38	71.13	187.965593	78.182777	12.284138	+16.931	271.335
Virgo A M87	2021-08-04	01:42:23.516-0000	42.38	71.13	187.965593	79.269077	12.284138	+16.129	272.060
Virgo A M87	2021-08-04	01:40:03.921-0000	42.38	71.13	187.965593	78.684146	12.284138	+16.561	271.670

Digitization Image Scale arcsec/pixel	Pixel Depth bits/pixel	Matrix Dimension Width (bytes)	Number of Rows	Exposure Time seconds	Local Observation Time Parameters Local Mean Sidereal Time 24h	Arrow of Time MJD	RA	HA	DEC
(11)	(12)	(13)	(14)	(15)	(16)	(17)	(18)	(19)	(20)
4.140	16	650	500	060.00	13:43:57	59430.068	12:31.86	05:12.73	+12:17.05
4.140	16	650	500	060.00	13:48:36	59430.071	12:31.86	05:17.08	+12:17.05
4.140	16	650	500	060.00	13:46:16	59430.069	12:31.86	05:14.74	+12:17.05

Local Time Elapsed Differences in UT	Technical Parameters Filter	Camera Status	Main Camera Focus	CCD Temperature Kelvin	Ambient Telescope Temperature Kelvin	Relative Humidity Percentage	Clear Sky Conditions 0-100
(21)	(22)	(23)	(24)	(25)	(26)	(27)	(28)
00:01:02.102-0000	Blue	Out	1350	000.0	299.0	38	000
00:01:02.104-0000	Red	Out	1350	001.0	300.0	18	000
00:01:02.103-0000	Green	Out	1325	003.0	300.0	33	000

Note—The series is not based on geocentric time but designed based on the induction of the local universe's order of astro-particle release, since M87 is a Kerr BH.

Table 1. Micro-Observatory Observations 2020 - 2021

Observed Object	Time of Observation Universal Time Date	Time	Observation Spatial Parameters Geographic Coordinate Latitude θ	Longitude λ	Spatial Direction RA	HA	DEC	Altitude & Azimuth α	γ
(1)	(2)	(3)	(4)	(5)	(6)	(7)	(8)	(9)	(10)
Virgo A M87	2021-08-04	01:40:03.921-0000	42.38	71.13	187.965593	78.684146	12.284138	+16.561	271.670
Virgo A M87	2021-08-04	01:31:32.956-0000	42.38	71.13	187.965593	76.628533	12.284138	+18.079	270.292
Dark A Caliberation	2021-08-04	04:00:24.143-0000	42.38	71.13	300.000000	1.866730	40.000000	+87.237	211.170

Digitization Image Scale arcsec/pixel	Pixel Depth bits/pixel	Matrix Dimension Width (bytes)	Number of Rows	Exposure Time seconds	Local Observation Time Parameters Local Mean Sidereal Time 24h	Arrow of Time MJD	RA	HA	DEC
(11)	(12)	(13)	(14)	(15)	(16)	(17)	(18)	(19)	(20)
4.140	16	650	500	060.00	13:46:16	59430.069	12:31.86	05:14.74	+12:17.05
4.140	16	650	500	060.00	13:37:44	59430.064	12:31.86	05:06.51	+12:17.05
4.140	16	650	500	060.00	16:07:00	59430.167	20:00.00	00:07.47	+40:00.00

Local Time Elapsed Differences in UT	Technical Parameters Filter	Camera Status	Main Camera Focus	CCD Temperature Kelvin	Ambient Telescope Temperature Kelvin	Relative Humidity Percentage	Clear Sky Conditions 0-100
(21)	(22)	(23)	(24)	(25)	(26)	(27)	(28)
00:01:02.103-0000	Green	Out	1325	003.0	300.0	33	000
00:01:02.063-0000	Clear	Out	1350	001.0	299.0	20	000
00:01:02.108-0000	Opaque	Out	1350	000.0	300.0	18	000

Note—From the variations in the experimental observation series and on the first M87 observation's long time gaps in the UT parameters in observation time, it can be inferred that the robotic parameters were set by the time domain of the black hole aspect of the Kerr.

Table 1. Micro-Observatory Observations 2020 - 2021

Observed Object	Time of Observation Universal Time Date	Time	Observation Spatial Parameters Geographic Coordinate Latitude θ	Longitude λ	Spatial Direction RA	HA	DEC	Altitude & Azimuth α	γ
(1)	(2)	(3)	(4)	(5)	(6)	(7)	(8)	(9)	(10)
Virgo A M87	2021-08-04	01:37:44.457-0000	42.38	71.13	187.965593	78.182777	12.284138	+16.931	271.335
Virgo A M87	2021-08-04	01:40:03.921-0000	42.38	71.13	187.965593	78.684146	12.284138	+16.561	271.670
Virgo A M87	2021-08-04	01:42:23.516-0000	42.38	71.13	187.965593	79.269077	12.284138	+16.129	272.060

Digitization Image Scale arcsec/pixel	Pixel Depth bits/pixel	Matrix Dimension Width (bytes)	Number of Rows	Exposure Time seconds	Local Observation Time Parameters Local Mean Sidereal Time 24h	Arrow of Time MJD	RA	HA	DEC
(11)	(12)	(13)	(14)	(15)	(16)	(17)	(18)	(19)	(20)
4.140	16	650	500	060.00	13:43:57	59430.068	12:31.86	05:12.73	+12:17.05
4.140	16	650	500	060.00	13:46:16	59430.069	12:31.86	05:14.74	+12:17.05
4.140	16	650	500	060.00	13:48:36	59430.071	12:31.86	05:17.08	+12:17.05

Local Time Elapsed Differences in UT	Technical Parameters Filter	Camera Status	Main Camera Focus	CCD Temperature Kelvin	Ambient Telescope Temperature Kelvin	Relative Humidity Percentage	Clear Sky Conditions 0-100
(21)	(22)	(23)	(24)	(25)	(26)	(27)	(28)
00:01:02.102-0000	Blue	Out	1350	000.0	299.0	38	000
00:01:02.103-0000	Green	Out	1325	003.0	300.0	33	000
00:01:02.104-0000	Red	Out	1350	001.0	300.0	18	000

Note—A duplicate piece of the previous Dark A calibration was sent in the data email. The design in my request was substituted with the amplification effect in the time domain adjusted by camera focus values, with time dilation.

Table 1. Micro-Observatory Observations 2020 - 2021

Observed Object	Time of Observation Universal Time Date	Time	Observation Spatial Parameters Geographic Coordinate Latitude θ	Longitude λ	Spatial Direction RA	HA	DEC	Altitude & Azimuth α	γ
(1)	(2)	(3)	(4)	(5)	(6)	(7)	(8)	(9)	(10)
Dark A Calibration	2021-08-04	04:00:24.143-0000	42.38	71.13	300.000000	1.866730	40.000000	+87.237	211.170
Virgo A M87	2021-08-04	01:37:44.457-0000	42.38	71.13	187.965593	78.182777	12.284138	+16.931	271.335
Virgo A M87	2021-08-04	01:40:03.921-0000	42.38	71.13	187.965593	78.684146	12.284138	+16.561	271.670

Digitization Image Scale arcsec/pixel	Pixel Depth bits/pixel	Matrix Dimension Width (bytes)	Number of Rows	Exposure Time seconds	Local Observation Time Parameters Local Mean Sidereal Time 24h	Arrow of Time MJD	RA	HA	DEC
(11)	(12)	(13)	(14)	(15)	(16)	(17)	(18)	(19)	(20)
4.140	16	650	500	060.00	16:07:00	59430.167	20:00.00	00:07.47	+40:00.00
4.140	16	650	500	060.00	13:43:57	59430.068	12:31.86	05:12.73	+12:17.05
4.140	16	650	500	060.00	13:46:16	59430.069	12:31.86	05:14.74	+12:17.05

Local Time Elapsed Differences in UT	Technical Parameters Filter	Camera Status	Main Camera Focus	CCD Temperature Kelvin	Ambient Telescope Temperature Kelvin	Relative Humidity Percentage	Clear Sky Conditions 0-100
(21)	(22)	(23)	(24)	(25)	(26)	(27)	(28)
00:01:02.108-0000	Opaque	Out	1350	000.0	300.0	18	000
00:01:02.102-0000	Blue	Out	1350	000.0	299.0	38	000
00:01:02.103-0000	Green	Out	1325	003.0	300.0	33	000

Note—Further analysis of the experiment needs to be confirmed by the image math algorithm

ISSN No:-2456-2165

Table 1. Micro-Observatory Observations 2020 - 2021

Observed Object	Time of Observation: Universal Time: Date	Time	Observation Spatial Parameters: Geographic Coordinate: Latitude θ	Longitude λ	Spatial Direction: RA	HA	DEC	Altitude & Azimuth: α	γ
(1)	(2)	(3)	(4)	(5)	(6)	(7)	(8)	(9)	(10)
Virgo A M87	2021-08-04	01:42:23.516-0000	42.38	71.13	187.965593	79.269077	12.284138	+16.129	272.060
Dark A Calibration	2021-08-04	04:00:24.143-0000	42.38	71.13	300.000000	1.866730	40.000000	+87.237	211.170
Virgo A M87	2021-08-04	01:40:03.921-0000	42.38	71.13	187.965593	78.684146	12.284138	+16.561	271.670

Digitization: Image Scale (arcsec/pixel)	Pixel Depth (bits/pixel)	Matrix Dimension: Width (bytes)	Number of Rows	Exposure Time (seconds)	Local Observation Time Parameters: Local Mean Sidereal Time (24h)	Arrow of Time: MJD	RA	HA	DEC
(11)	(12)	(13)	(14)	(15)	(16)	(17)	(18)	(19)	(20)
4.140	16	650	500	060.00	13:48:36	59430.071	12:31.86	05:17.08	+12:17.05
4.140	16	650	500	060.00	16:07:00	59430.167	20:00.00	00:07.47	+40:00.00
4.140	16	650	500	060.00	13:46:16	59430.069	12:31.86	05:14.74	+12:17.05

Technical Parameters: Local Time Elapsed (Differences in UT)	Filter	Camera Status	Main Camera Focus	CCD Temperature (Kelvin)	Ambient Telescope Temperature (Kelvin)	Relative Humidity (Percentage)	Clear Sky Conditions (0-100)
(21)	(22)	(23)	(24)	(25)	(26)	(27)	(28)
00:01:02.104-0000	Red	Out	1350	001.0	300.0	18	000
00:01:02.108-0000	Opaque	Out	1350	000.0	300.0	18	000
00:01:02.103-0000	Green	Out	1325	003.0	300.0	33	000

NOTE—This Dark A data has the same parameters with the last one, although with email feedback separately in another groups of RGB data.

Table 1. Micro-Observatory Observations 2020 - 2021

Observed Object	Time of Observation: Universal Time: Date	Time	Observation Spatial Parameters: Geographic Coordinate: Latitude θ	Longitude λ	Spatial Direction: RA	HA	DEC	Altitude & Azimuth: α	γ
(1)	(2)	(3)	(4)	(5)	(6)	(7)	(8)	(9)	(10)
Sun	2021-09-15	18:00:08.984-0000	42.38	71.13	173.670954	20.151214	2.734154	+46.455	209.966

Digitization: Image Scale (arcsec/pixel)	Pixel Depth (bits/pixel)	Matrix Dimension: Width (bytes)	Number of Rows	Exposure Time (seconds)	Local Observation Time Parameters: Local Mean Sidereal Time (24h)	Arrow of Time: MJD	RA	HA	DEC
(11)	(12)	(13)	(14)	(15)	(16)	(17)	(18)	(19)	(20)
5.160	16	650	500	000.25	08:54:37	59472.750	11:34.68	01:20.60	+02:44.05

Technical Parameters: Local Time Elapsed (Differences in UT)	Filter	Camera Status	Main Camera Focus	CCD Temperature (Kelvin)	Ambient Telescope Temperature (Kelvin)	Relative Humidity (Percentage)	Clear Sky Conditions (0-100)
(21)	(22)	(23)	(24)	(25)	(26)	(27)	(28)
00:00:02.291-0000	Grey (ND4)	High	none	287.0	316.0	53	093

NOTE—The sun observation used solar tracking with the center of main camera in finder camera on 377, 239. Another experimental group of observation on M87 is not listed here and would require another article for specific analysis.

II. METHODOLOGY

The four laws of BH mechanics puts the threshold of fission on $0K$ as the instrumentation security protocol.[2] It means that the photometers on the imaging plate is dependent on the chemical dynamics of the wells that determine the quantum potentials on space telescopes. The force analysis on the quantum potentials largely determines the reading on local chemical dynamics as the astrochemical supplement to astrophysics.[20] The numerical methods on quantum forces with photo-metric data provides with the basics on quantum cosmology. The author introduced Hamiltonian zero $\vec{0}$ for the purposes on quantum cosmological induction.[15] With this rationale, the Bekenstein-Hawking entropy formula and Einstein's equation are combined in the context of special relativity $S = \frac{\pi Ak\sqrt{E^3}}{2hG\sqrt{M^3}}$. This equation form does not suppose the chemistry type of any given object, i.e. how many times of critical mass the source WHs have reached.

With the context, each pixel on the imagery data is read as a three-dimensional time, and the extensions of time is processed as spatial distribution with either bitpix or brightness. Therefore, in the original Bekenstein-Hawking entropy formula $S = \frac{\pi Akc^3}{2hG}$, one fraction of the time denoted by c is with brightness, another with pixel depth, and one with the World Coordinate System (WCS).[17] The direct observation on the energy fractions of the mass presupposes the mass-energy symmetry by $\sqrt{(\frac{E}{M})^3}$, and the asymmetry of all forms of matter in the local universe. Therefore, the lower the luminosity, the more precise the quantum state.[8] However, the limitations on instrumentation still resides with the annihilation of quantum states to the actual developments of the celestial objects. The cosmological constant $P = -\frac{\lambda}{8\pi}$ thus substitutes for the scales of dimensional lengths, and the density of the BH ρ is introduced by the volume of the black hole V to the variant $S = \frac{\pi AkEc}{2hGM}$ and written as $S = \frac{\pi AkE^2}{2hGM\rho}$. Whereby the two-dimensional entropy for the Schwarzschild radius can be written as $S = \frac{\pi AkMc}{hr_0}$, with c denoting the spectral information arrived at the quantity with the speed of light, the incompleteness on the BH theories is at the core on quantum gravity.[18]

The observational experiment went in parallel with the data analysis on NGC 3034 with a Kerr-Newman case, and the Einstein field equation (EFE) $G_{\mu\nu} + \Lambda_{\mu\nu} = \kappa T_{\mu\nu}$ was adopted for the reading on the heliocentric Chandra X-ray space tele- scope.[16] The multi-spectral kinematics is processed as seen in *Figure 2*. The Einstein gravitational constant denoted by κ with Newtonian gravitation can be adopted as galactic projection from the solar system to induce the black hole's trace signature with surrounding spatial objects $\kappa = \frac{8\pi G_n}{c^4}$, therefore, for the instrumentation security the Schwarzschild radius solution can be used as a negative time modeling technique in the fraction of black hole development and historical development in an idealized conceptual model. The EFE $R_{\mu\nu} - \frac{1}{2}Rg_{\mu\nu} + \Lambda g_{\mu\nu} = \kappa T_{\mu\nu}$ can be used with a time dilation from the mass r_0 to R to a Reissner-Nordström BH model and the resonance observation is animated in the video.[14] To emphasize on the fundamental symmetry & asymmetry question's importance in astrochemical inquiries and quantum cosmology, a similar technique with Daly's approach is used by replacing the K terms with the κ terms as $S = \frac{4\pi^2 AEG_{n-1}}{hMc^3}$ & $S = \frac{4\pi^2 AE^2 G_{n-1}}{hMc^3\rho}$. Therefore, for the BH in the Schwarzschild radius solution it is $S = \frac{8\pi^2 AMG_n}{hr_0 c^2}$, which also underlines the reason for the introduction of Hamiltonian zero to the operation.[4]

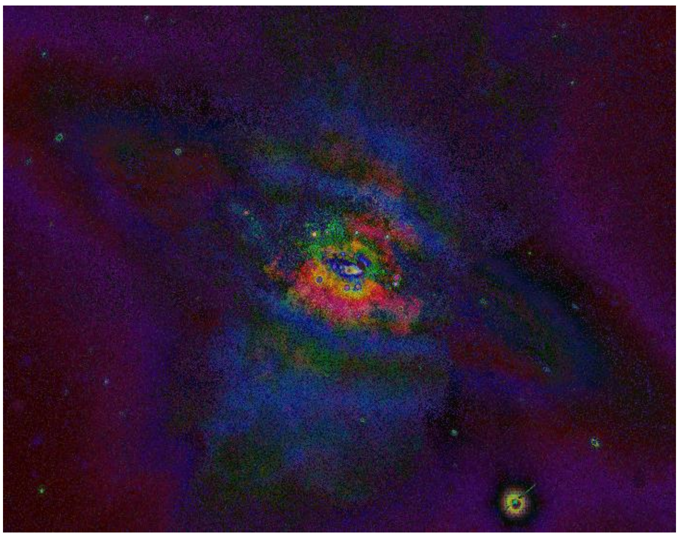

Fig. 2: The multi-spectral kinematics data rendition on NGC 3034 Kerr-Newman BH.

III. THE JUXTAPOSED BLACK HOLE AND WHITE HOLE

Inductively, suppose with Newton's Law of Universal Gravitation, the number of faces F ∈ ∞ describes space-time fabric, the number of verticals V are unidirectional time to the vortex of the black hole singularity (BHS) and the angular momenta of the astro-particles' inertial speed, the sum of edges $E \in \infty$ describes the total kinetic energy momenta distribution towards BHS by the astro-particles in the vicinity of a BH. In the context of conservation of mass, i.e. conservation of energy, the macroscopic coordinate system on the vortex of a BHS on the outer surface can thus be described as:

$$E = F + V - 2 \equiv M_v c^2$$

with equivalence to Bolometric luminosity (1)

With a binary rationale based on the MacOS computer the author was using, the "1 + 1 = 2" question was reformulated as:

$$(cos\alpha + sin\alpha) + (cos\beta + sin\beta) = F + V - E \qquad (2)$$

For that the oscillation of BH & WH makes the BHS highly unstable chemically and moving through time, the exterior space-time between the Kerr-Newman Black Hole (KNBH) and its vicinity $M_{BH} \cap M_{VIC}$ on the limit of the BHS in relation to the gravitational singularity as in the interior space-time $\tau \in M_{BH}$, the entropy and instrumentation security are integrated to:

$$\textbf{Theorem 1}\ (\cos\alpha + \sin\alpha) \vee (\cos\beta + \sin\beta) + \vec{0} \begin{cases} = F + \vec{V} - E \\ \leq F + V - E \end{cases} \alpha \geq \beta \qquad (3)$$

The gravitational well caused by WH emitting from the juxtapose forms the dark matter halo and dwarf galaxies with shock-waves causing optical and ultraviolet flares, and the multispectral presentation is shown in *Figure 3*.[12] Such shock-waves' direct influence to the sun is apparent in the observational result shown in *Figure 4*, and can be the cause for Eddington luminosity expressed in *Equation 1*. Dark matter and anti-matter are not included in the theory and replaced by the WH material. The low luminosity of the LSB galaxies and the dark star postulate thus can be explained by the deep electron orbit theory on a macro-particle sense with differentiation in thermodynamics and oscillation on quantum levels in all of the BH types with *Figure 5* as the KN example.[15][11] It is also in this sense, the electromagnetic pulsating received by data signal or image noises are the multi-spectral frequency indicators on the most fundamental instrumentation level regarding the deep electron orbit theory.[7] The electromagnetic properties among electron and anti-electron combinations are key to further insights into the quantum properties of the galactic electron explosions.

Fig. 3: The momentum on the gravitational well on NGC 3034.

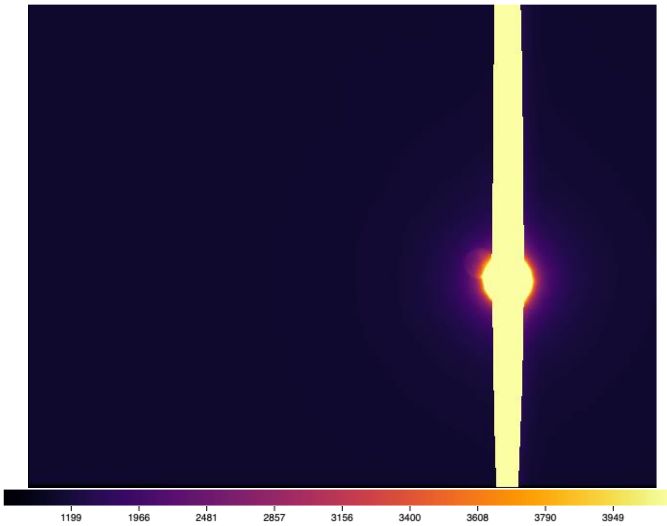

Fig. 4: The tidal lock's impact on the sun.

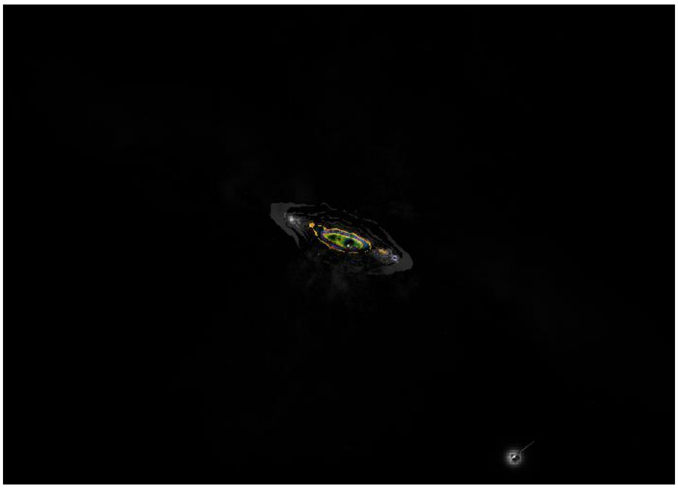

Fig. 5: The WH material fields on NGC 3034.

Albeit the instrumentation orbits were different, the computer-based analysis only focused on the signal rates as light source (light signal) for the information theory for the observer on the inducted quantum metric on the time-asymmetry of the KNBH. It aimed at finding the BHS as the portal for the WH with the judgement for it to be a KNBH.[16]The second term of the theorem thus holds that

ISSN No:-2456-2165

the actual spatial energy will always be greater than the received time-frames of references, and considered the four laws of BH mechanics as systemic threshold as expressed in *Theorem 1*. It then used Traver's reworded postulates on Euclid's five postulates to simplify the forces involved in the celestial body, with $\vec{V} \in M_{BH}$, $\tau_n \in F$, $t_n = F \cap \vec{V}$, and $n \geq 0$.[19] The gravitational singularity is denoted by S.

REWORDED POSTULATE	**APPLICATION IN THE FRAMEWORK**
For every point $P$and for every point Q not equal to P, there exists aunique line$l$ that passes through P and Q.	For the consecutive movement of a BH singularity S in time with or without exchange of energy, and for any specific astro-particle P inits vicinity, there exists a unique line f thatpasses through S and P.
For every segment AB and for everysegment CD, there exists a uniquepoint E such that$B$ is between$A$ and$E$ and segment CD is congruentto segment BE.	For every segment $S_{t(n)}P_{t(n)}$ and for everysegment $S_{t(n-1)}P_{t(n-1)}$ there exists a uniquepoint $\tau_{t(n)}$ such that $P_{t(n)}$ is between $S_{t(n)}$ and $\tau_{t(n)}$ and segment $S_{t(n-1)}P_{t(n-1)}$ is congruentto segment $P_{t(n)}\tau_{t(n)}$.
For every point O and every point$A$ not equal to O, there exists a circlewith center O and radius OA.	For every point of a BH mass center M andevery point $S_{t(n)}$ not equal to M, there existsa circle with center M and radius $MS_{t(n)}$.
All right angles are congruent toeach other.	All right angles on the same plane are congruent to each other.
For every line l and for every point P that does not lie on l, there existsa unique line m through P that isparallel to l.	For every line *f(t)* and for every point P thatdoes not lie on *f(t)*, there exists a unique line $M_{t(n)}$through P that is parallel to *f(t)*.
Traver's reworded Euclid's five postulates stated geometric congruences that is measurable and can bequantified.	**The static postulates are put into a unidirectional timeframe of spacetime for empirical determination on weak force torque of a BH's singularity.**

IV. EXPANSION OF EUCLID'S FIVE POSTULATES

The aspect of the WH is extended with the trigonometrical functions of β and hereby replaced with θ for the observer as in the non-locality principle by David Bohm. Therefore, every face the distribution of the astro-particle has an angular momentum θ to the singularity vertex, and$\cos\theta$ describes the distance between the astro-particle and singularity at the $\tan\theta$position of the observer, for that there is only one event that actually exists and observed by the observer. Since there is only one true state of theastro-particle in question, the dimensional distribution of the astro-particle can be written as $\cos F\theta$. And this is the distance between the astro-particle and singularity. $\sin\theta$ is written for the observed distance between the astro-particle and singularity. The dimensional aspect of the observed distance is thus $\sin F\theta$. The distance between the astro-particle and singularity observed can thus be written as $\cos F\theta + i \sin F\theta$, or with de Moivre's formula to the Euler's identity:

$$(\cos\theta + i\sin\theta)^F = e^{iF\theta} \equiv inertial\ mass\ distance \tag{4}$$

The three-body problem in this formula is then between the entropy of the BH and the inducted state of the WH. i is used here to denote the extended dimension of time from the reference frame and further mathematical alterations can be adapted according to the quantum developments as suggested in *Theorem 1*. The juxtaposed pair $\sum_{\theta=\beta}^{\gamma} e^{iF\theta} \propto \infty$ describes the simultaneity of the multi-spectral sources observed and the astro-physic-chemical aspect underlying the event. This is to state the eternal black hole theory based on the surface area law, with V describing the inertial state of the astro-particles. [9] Since the observed frame of reference is from unlocked emissions, the energy trail of time to the BH spin is thus:

$$\textbf{Theorem 2}\quad F = \begin{cases} \frac{1}{2}\ln\frac{1+\theta}{1-\theta} = \arctan^{-1}\theta & \textit{WH induction} \\ \frac{1}{2}\ln\frac{1+c}{1-c} = \arctan^{-1}c & \textit{observed entropy} \end{cases} \tag{5}$$

From the local universe to the geocentric reference system where Chandra was on highly elliptic orbit, the description of the singularity of the multidimensional time in the frame in reference to *Theorem 2* and *Figure 5* can thus be written as:

$$\textbf{Theorem 3}\quad \vec{V} \propto \begin{cases} (c - e^{iF\theta})(c + e^{iF\theta}) = c^2 - \frac{1+\theta}{1-\theta}e^{i\theta} = c^2 - \frac{1+\theta}{1-\theta}\operatorname{cis}\theta \\ c^2 - \frac{1+c}{1-c}\operatorname{cis}\theta \quad \textit{entropy observed as radiated chemical light} \end{cases} \tag{6}$$

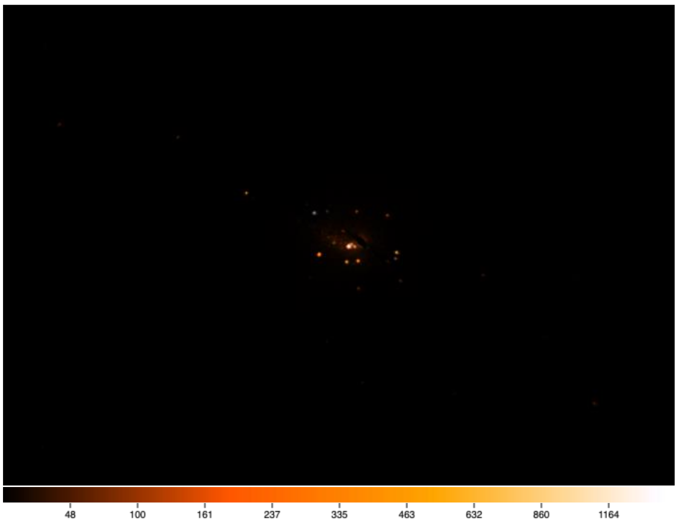

Fig. 6: The X-ray reference frame on NGC 3034 blended with luminosity; High, mid, and low energy from 700 to 6000 eV, Chandra; Galactic l~+141:24:42.996 b~+40:33:52.780.

Since the observed charge of the KNBH-WH is transmitted in vacuum and captured by space telescopes, the observed event's neutron weak force interaction between the BH and its vicinity shapes the dynamic singularity of the KNBH by the second term of $\vec{V}$. This expression eliminates the presumption of an inertial reference to the juxtaposed charged body and its vicinity as a whole, the currently unobservant center, and the traditionally globular presumption of a BH in mathematical expressions. In relation to multi-spectral surveys, all wavelengths travel at the same speed in vacuum except for the astro-particle interactions producing the emissions. The compound Chandra X-ray reference frame provided the case for the vicinity of NGC 3034's radial emission and surface momentum of the spinning KNBH-WH, the JS9-4L processed heliocentric Spitzer Space Telescope's infrared samples show the electron weak force surface as the ring singularity as shown in *Figure 7*.[16]

Fig. 7: Spitzer mid and near infrared with ring singularity as decayed reference framefor gravitational singularity in $asinh\,\theta$.

For the empirical Newtonian terms, with the geocentric radius of the earth as r, the torque of the α and β decay is thus $\tau = rF\sin\theta$ for Chandra X-ray data. In the electromagnetic congruence of the BH vicinity, let the infrared reference frame's BHradius be r_{BH} and its inertial mass be M_v, with f denoting the second term of F, and V denoting the second term of $\vec{V}$; the torque of $m_v \in M_v$ on the coordinate system would be (with the second term in reference to *Equation 1*):

$$\textbf{Theorem 4}\quad \tau_{M_v} \equiv \begin{cases} r_{BH} f \sin(1-\theta) = r_{BH} f \cos\theta \\ \textit{The decay angle of emission is equivalent to Hawking radiation} \\ E = m_v F^2 V^{-2} \\ \textit{the two terms are theoretically interchangeable with symmetry presumption} \end{cases} \tag{7}$$

Without accounting for the inducted gamma ray, and without correction on the space telescopes' differences in orbit, cosmic expansion rate, and the deployed mission cycle, the equilibrium state of the quantum force space-time on the infrared reference frame is:

$$M_v \begin{cases} = (F + \vec{V} - 2)(\frac{V}{F})^2 & = (\arctan^{-1}\theta + c^2 - \frac{1+\theta}{1-\theta}\operatorname{cis}\theta - 2)(\frac{c^2 - \frac{1+\theta}{1-\theta}\operatorname{cis}\theta}{\arctan^{-1}\theta})^2 \\ > \frac{EV^{-2}}{F^2} & = \frac{e^{i\theta \arctan^{-2}\theta}(c^2 - \frac{1+c}{1-c}\operatorname{cis}\theta)^{-2}}{\arctan^{-2}\theta} \quad \text{the moon observation} \end{cases} \tag{8}$$

Thus, the prerequisite on the experimental observation was set as shown in *Equation 8*, and the above equation with *Theorem 4*describes the all-wavelength decay from the data shown in *Figure 8*. And the whole set for the expressions on the juxtaposed observation can thus be expressed as:

$$\textbf{Theorem 5}\quad (\cos\alpha + \sin\alpha) \vee (\cos\beta + \sin\beta) + \vec{0} \begin{cases} = F + \vec{V} - E + M_v \\ = (F + \vec{V})[1 + (\frac{V}{F})^2] - [E + 2(\frac{V}{F})^2] \\ = \arctan^{-1}\theta + c^2 - \frac{1+\theta}{1-\theta}\operatorname{cis}\theta - M_v(\frac{\arctan^{-1}\theta}{c^2 - \frac{1+\theta}{1-\theta}\operatorname{cis}\theta})^2 \\ = 2 \end{cases} \tag{9}$$

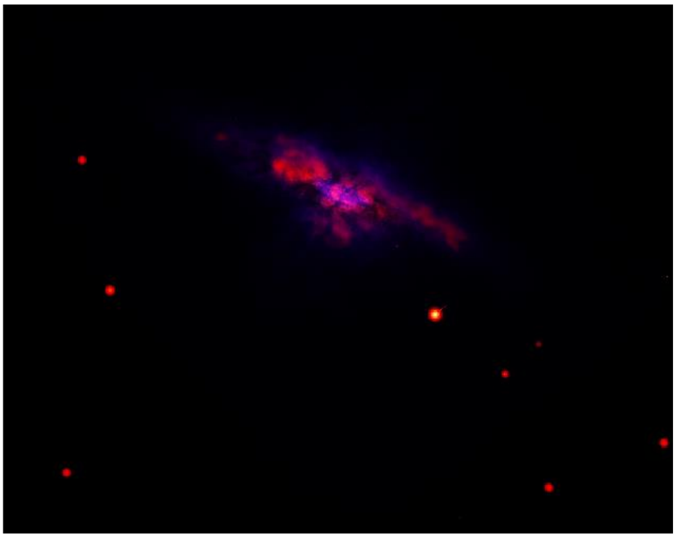

Fig. 8: The torque decay momentum of the Kerr-Newman on NGC 3034 through the weak force slit.

Hereby the numerical values of 1 and 2 represents macro-particle energy tensors and corresponds to $\vec{0}$. Therefore, empirical WH insertion into the instrumentation system will not destructively affect the existing

ISSN No:-2456-2165

instrumentation systems, including the in- sertion of gamma rays that the data currently lack. $(V - i)(V + i)$ is the bottom-up centrifugal force corrector to the existing data system as space-time complement for instrumentation security as shown in *Figure 5*.

V. OBSERVATIONAL RESULTS

The observation report on a reversal time order from the observation sequence. The observation directly observed the sun's imprint from the distant strong force's influence. The angular sizes of the two imprints suggest there are two main tidal forces that contribute to the phenomenon shown in*Figure 8*&*Figure 9*. The direct force formed the imprint of the sun by the side of the main image with high surface brightness and belongs to the fusion force. The other force has clear resonance effect on the sun and formed a distant image. The fission force has stronger impact on the sun and may be the major contribution to the solar wind.

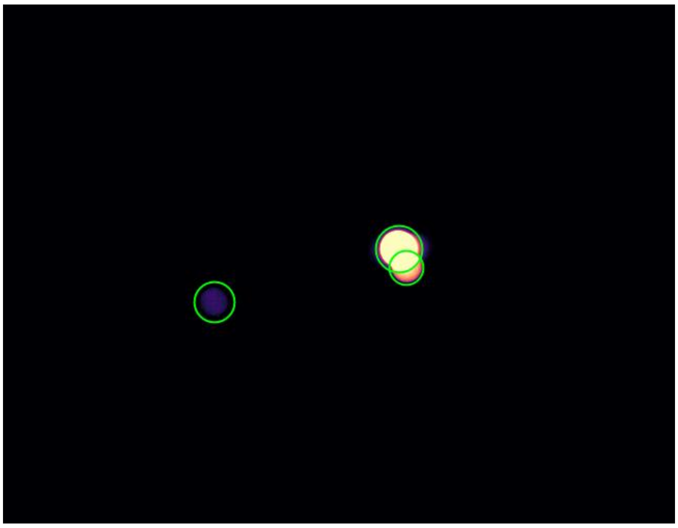

Fig. 9: The sun's imprint from the BH-WH juxtapose nuclear influence.

In the Trifid Nebula M20 observation, the source contains a highly luminous center of explosion with gas vapors as shown in *Figure 10*. The jets exploded from the central crystal formed both high luminous globular shaped seeds and BH seeds. This means that the crystal center observed is not a direct observation on the BH. The neutron star as a possibleremnant from the oscillation as WH seed and the graphite suggested by the forking of ultraviolet light may be a contribution to the occultation of WH from being detected. From chemical induction, similar structures to vantablack can be a product from the WH-BH oscillation that underlies the dark matter and dark matter halo as shown in *Figure 10*. From the hot dark matter data reduction, the shredded metallic pieces are thermally constant to radiation in the below *0K* environment. The fission influence is both consistent to the NGC 3034 data with the crystallization effect and a later stronger imprint observation on the sun.[15]

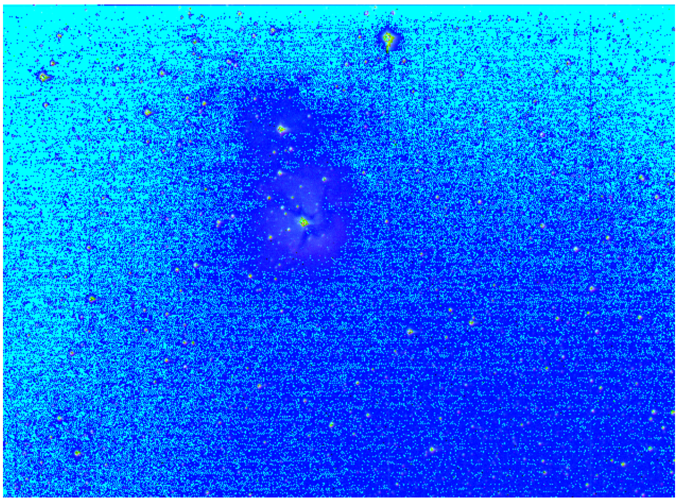

Fig. 10: The high noise processed data on the Trifid Nebula M20.

The direct observation on the WH took place on the moon observation with the sun as shown in *Figure 4*. The WH is hidden from view in the data, and the processing used strong amplification on the quantum effect shown in *Figure 1*. The main source in the observation becomes visible with a mean value of 1689.20 on a gauge boson background. The author controlled the quantum limits on vector bias in the field and sought the source for the solar wind scalar bosons with rms 966.19. The result is consistent with the 3dPlot on spatial curvature of the source in linear direction in physical location (475, 319). The main luminosity source has a mean value of 3806.89, and the moon 3009.45. With regression analysis on rms values, the moon (886.19) is closer to the observational apparatus than the sun (501.79). The sun in the observation is composed of scalar bosons. The author shifted the quantum effect and the main source in the observation becomes visible with a mean value of 1689.20 on a gauge boson background. A mildly processed graphics is included as *Figure 12* for the energy traces on the observation. It means that the moon's imaging is from the fusion storm caused by the fission activities of the WH as shown in *Figure 4*.

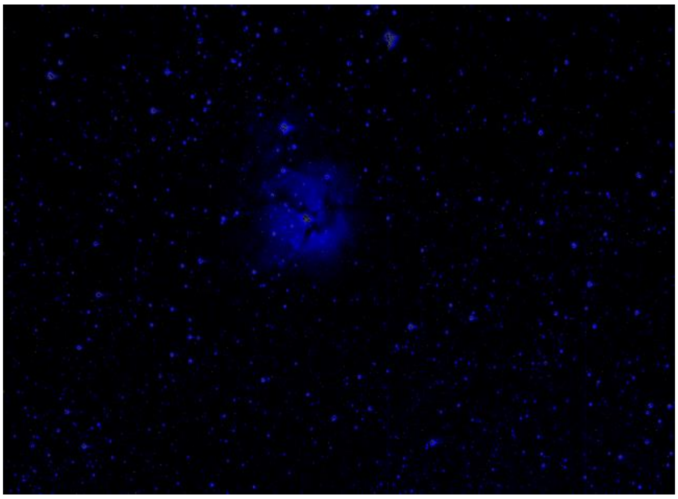

Fig. 11: The cold dark matter presentation of the Trifid Nebula.

ISSN No:-2456-2165

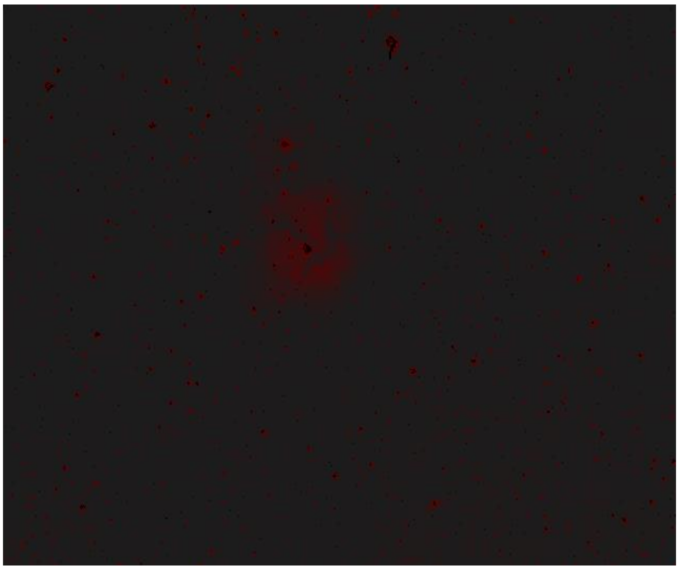

Fig. 12: The hot dark matter presentation of the Trifid Nebula.

Hereby the scalar bosons can be seen as a curved z plane in relation to the *f*(*x*,*y*) gauge boson vector plane. The scalar curvature in question has three intersecting points as the mass source to the gauge boson plane in the spatial vector dissecting on the physical location *p*(*x*, *y*) of the morphological mass-spatial centers. The mean values and rms values are not corrected to the gravitational pressures whose phenomenology is visible as the solar wind. The mean curvature of the space then can be described as the co-variance between the two functions on the numerical values. The curvature ratio of each point as in the distance in the depth of view is expressed as:

Proof 1 $d_z = \binom{mean}{rms}$ (10)

The value on the distance of the sun, the moon, and the source object affecting spatial curvature is respectively 7.58662, 3.595942, and 1.74831037.5 The fast solar wind radius in the concentric purple circle in *p*(*x*,*y*) = (497,214) has a value $d_z = 1.942165$, which is caused by the point rotations between the gauge field and scalar fields, and thus gives the distance bias to the curvature source to $d'_z = 0.193855$.

The peak λ curvature of the source is around 65, with the moon's peak in 15 and the sun's around 14. The above equation expresses the spatial curvature on the y axis in relation to $p(x, y)$ as expressed in *Proof 1*:

Proof 2 $d_{y'} = \binom{\lambda}{d_z}$ (11)

This gives the source point's curvature to 37.17875 as compared to the sun 1.845354 and the moon 4.171369 as expressed in *Proof 2*. The mean average of the moon and the sun is 2.9525684. Since the value of d_z is given, the trigonometrical relations on $d_{y'}$ in the observation is $\Delta d_{z_1} d_{z_2} d_{z_3} \cong \Delta \lambda_1 \lambda_2 \lambda_3$, which means the time-dependent values of λ is congruent to curvature length. A transitional coordinate is given as $f'(x, y) = (d_z, d_{y'}) \cong p(x, y)$. With the physical location values $p_{moon} = (468,233)$, $p_{sun} = (497,214)$, and $p_{source} = (475,318)$, the projected spatial values $f'(x, y)$'s distances are derived with SSS congruence theorem as $d_{moon-sun} = 4.61907530572$, $d_{moon-source} = 33.0590523627$, and $d_{source-sun} = 35.81249408$. The distance bias in the projected coordinate $f'(x, y)$ can be gotten with the baseline ratio of the moon-sun relation to the physical locations as 7.50580351088. The bias ratio of the moon- source and sun-source distances are respectively 2.5798606477 and 2.96827855356. The bias results mainly come from the incomplete transformation of $d_{y'} \to d_y$, and the limit is set by λ. Replacing p_y with λ, $|d_{moon-sun}| = 29.0172362571$, $|d_{moon-source}| = 50.4876222455$, and $|d_{source-sun}| = 55.542776308$. This gives corrected biases respectively to 6.28204442157, 1.52719508386, and 1.55093292815. This proves the λ limit corrects the spatial curvature to the distant source projected as d'_z. Replacing p_x with d_z, the biases correct to $|d_{moon-sun}| = 4.11406257848$, $d_{\text{moon-source}} = 50.0341257807$, and $|d_{source-sun}| = 51.3330873739$. The check for proof bias is given:

$$\textbf{Bias Factor} \lim_{n \to 1} f(n) = (d'_z + n) \frac{d_p}{d_{p'}}$$

(12)

Without the corrective $(d'_z + 1)$ factor, the values are 1.12275280641, 0.660730088652, and 0.697649331301. With the $(d'_z + 1)$ factor, the values are 1.3404040517, 0.788815919987, and 0.83289214242. Thus, the z plane coordinate in reference to *Theorem 5*can be expressed as:

Theorem 6 (Adjusted coordinate for mean spatial curvature)

$f(x, y) = \left(\binom{mean}{rms}, \lambda\right)$ (13)

With the decayed limit, the mathematics suggest that the binary observation on the WH with the moon observation is probable. It suggests that even though the WH-BH juxtapose space-time may have similarities to the Big Bang space-time model,the differences lie with the condensed matter physics epistemology in the Big Bang model.

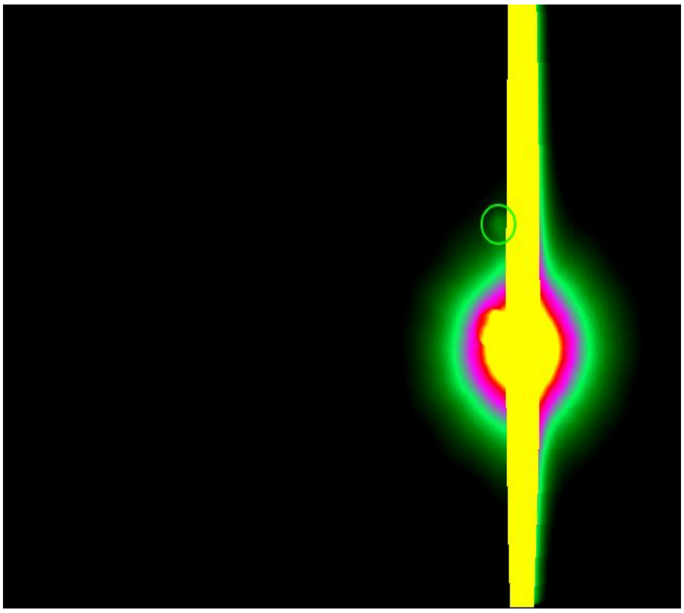

Fig. 13: Direct observation on the gravity curved space and the source of spatial curvature.

ISSN No:-2456-2165

VI. CONCLUSIONS

The experimental result suggests with solar object lens effects, combinations of observation with ground-based telescopes and space-based telescopes are possible. The inverse factors in the depth-of-view influenced the solar wind and the peak eruption, whose shape was influenced by the gravitational effect on bosons, with the shift slightly hinting its existence shown in *Figure 14.* The crystallization effects and graphene can be the two major influences to the currently undetected gravitonsapart from the thermo-eruptions. By the observations from Southern Pinwheel on, the evidence for the BH-WH juxtapose theory is experimentally and empirically proved.

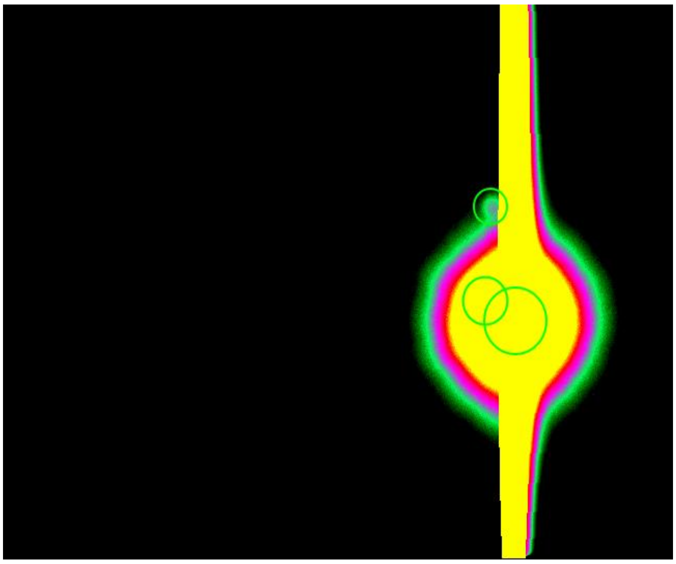

Fig. 14: The resonance effect between the moon-sun system and the probable WH.

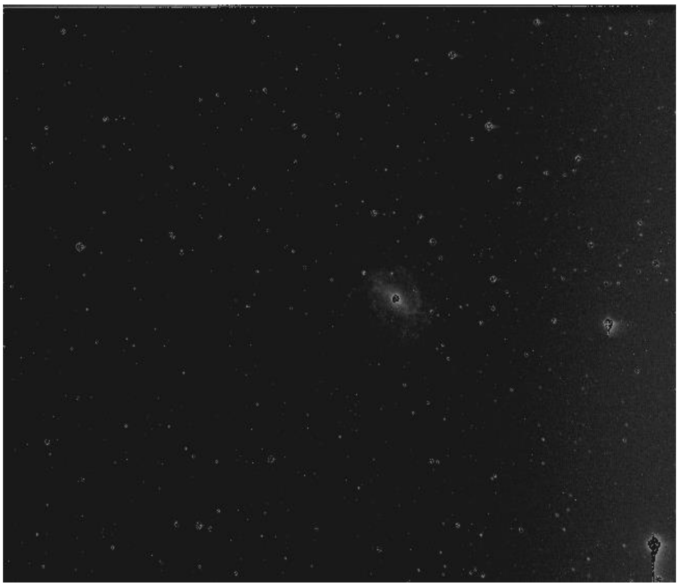

Fig. 15: The BH with thermal influence on Southern Pinwheel.

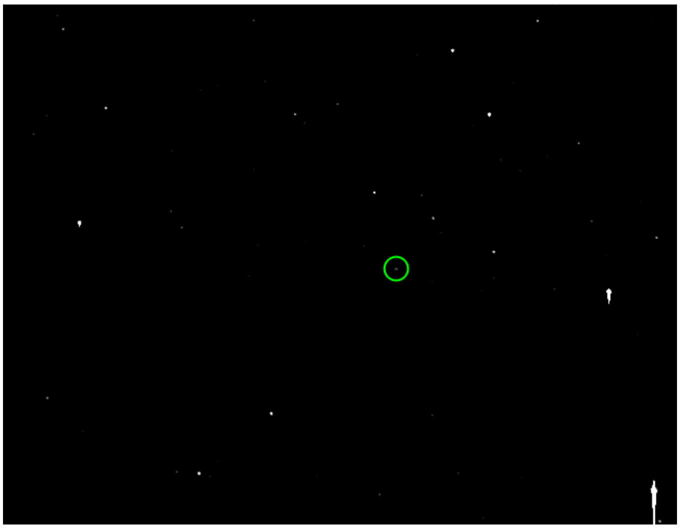

Fig. 16: The galactic nuclei on Southern Pinwheel.

Fig. 17: The (future) light cone on Southern Pinwheel.

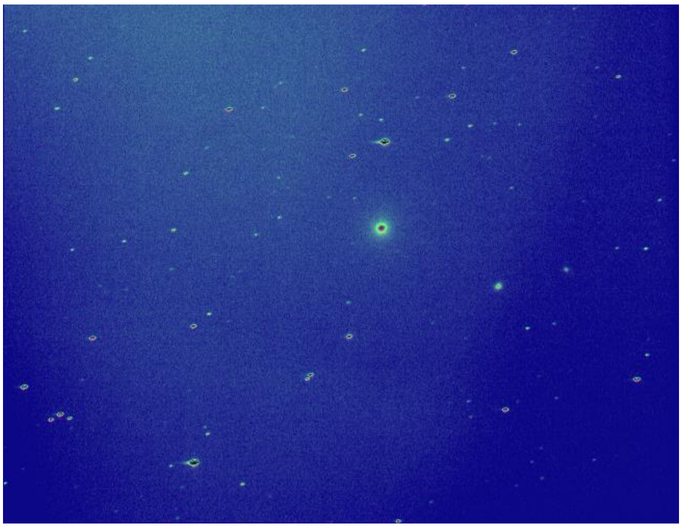

Fig. 18: The BH on M87.

ISSN No:-2456-2165

Fig. 19: The space and time like singularity on M87.

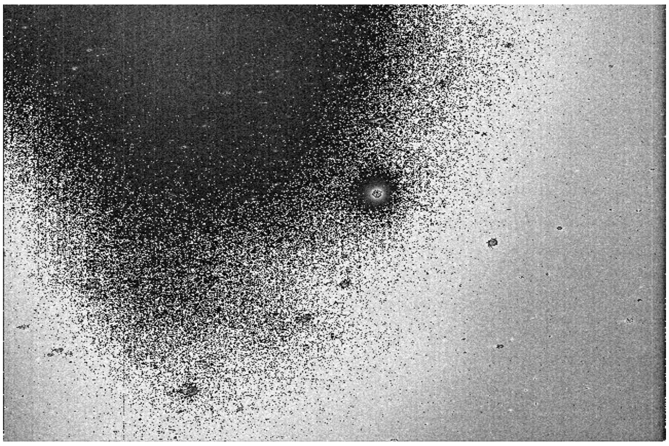

Fig. 10: The WH on M87 with high noise.

VII. APPENDIX

This research is based on observations made with the NASA/ESA Hubble Space Telescope obtained from the Space Telescope Science Institute, which is operated by the Association of Universities for Research in Astronomy, Inc., under NASA contract NAS 5–26555.

This research is based on observations made with the Galaxy Evolution Explorer (GALEX) satellite, a NASA mission led by the California Institute of Technology, obtained from the Space Telescope Science Institute, which is operated by the Association of Universities for Research in Astronomy, Inc., under NASA contract NAS 5–26555.

The scientific results reported in this article are based [in part] on observations made by the Chandra X-ray Observatory.

This work is based [in part] on observations made with the Spitzer Space Telescope, which was operated by the Jet Propulsion Laboratory, California Institute of Technology under a contract with NASA.

The observations are performed on Harvard-Smithsonian Micro-observatory, andthe data are processed by JS9-4L online and SAO Image DS9 MacOS.[6][3]

ACKNOWLEDGMENT

The author would like to thank University of Arizona who offer the course *Astronomy: Exploring Time and Space* via *Coursera.org*, and the constant guidance offeredby professor *Chris David Impey*. With the companionship of the *Teaching Astronomy* team *Mathew Wenger*, *Victoria Pereira*, and *Michael Hardegree-Ullman*, the author went through the most difficult times while keeping up with the up-to-date news on the astronomical development. *Grant Bowman*'s mimics is as cheerful as the clown master *Christopher Bayes*' classes that made the astronomy streams fun and flourishing. It was by *ArunaPawashe*'sinvitation to Yale Chaplain's office the author regained his spirit in the astrophysical sciences and he is still grateful. It was by the encouragement of *Roger Penrose* on the webinar *Science and Roger Penrose* the author started to learn to speak out his mind publicly and with other speakers' presentations that corroborated with the observational judgements. Meanwhile, the *Facebook* group *IQ Test & Fun* and the quantum sciences groups exercised the author's brain while reformulating the mathematics, and the author is proud to be a member. The author was supported intellectually by the *Astropedia* Discord server group during the Odyssey learning to write in *LaTex* and the observations. The author feels grateful to the support teams and engineers behind the instrumentation whose names the author may not have a direct knowledge of but constantly felt their presence and support. Last but not least, the author is grateful for his parents' constant support and sheltering, without which the years of research and writing could not have resumed. The author is deeply thankful for his not yet governmentally enacted husband for his patience and understanding. And I adore his psychological and sociological approaches in serving the LGBTQI community worldwide.

REFERENCES

[1.] Bagla, J. S. (2020).Compact Objects and Black Holes: Nobel Prize for Physics 2020. https://arxiv.org/abs/2012.08774
[2.] Bardeen, J. M.,Carter B., and Hawking, S. W. (1973).The Four Laws of Black Hole Mechanics, Communications in Mathematical Physics, 31, 161, doi: 10.1007/BF01645742
[3.] Bertin, E., &Arnouts, S. (1996). A&AS, 117, 393, doi: 10.1051/aas:1996164
[4.] Daly, R. A. (2009). in American Institute of Physics Conference Series, Vol. 1166, Sources and Detection of Dark Matter and Dark Energy in the Universe, ed. D. B. Cline, 81–86, doi: 10.1063/1.3232198
[5.] Depuydt, L. (2021).The Physical Laws and Mathematical Axioms of the Brain's OS and the Traditional Fundamental Laws of Thought of Logic and Philosophy. Advances in Pure Mathematics, 11, 988, doi: 10.4236/apm.2021.1112064
[6.] Ferland, G. J., Porter, R. L., van Hoof, P. A. M., et al. (2013). The 2013 Release of Cloudy,RMxAA, 49, 137. https://arxiv.org/abs/1302.4485
[7.] Gaskin, J. (2022).LYNX X-ray Observatory Concept Study Report (NASA). https://wwwastro.msfc.nasa.gov/lynx/docs/LynxConceptStudy.pdf

[8.] Greg Bothun, Chris Impey, S. M. (1997). Hidden Galaxies Revealed. https://citeseerx.ist.psu.edu/viewdoc/ download?doi=10.1.1.254.9320&rep= rep1&type=pdf
[9.] Hawking, Stephen W., Perry, Malcolm J., and Strominger, Andrew (2016). Soft Hair on Black Holes. Phys. Rev. Lett., 116, 231301,doi: 10.1103/PhysRevLett.116.231301.
[10.] Hsu, S. D. H. (2011).Classical and Quantum Gravity, 29, 015004, doi: 10.1088/0264-9381/29/1/015004
[11.] Kodama, Noriyuki. (Volume. 7 Issue. 1, January - 2022) "Possibility of Transmutation to Super Heavy Element by Cold Fusion Mechanism.", International Journal of Innovative Science and Research Technology (IJISRT), www.ijisrt.com. ISSN - 2456-2165 , PP :- 11-18.
[12.] Mahler, G., Natarajan, P., Jauzac, M., & Richard, J. (2022).Gravitational lensing effects of supermassive black holes in cluster environments. https://arxiv.org/abs/2201.10900
[13.] Natarajan, P., Sigurdsson, S., & Silk, J. (1998).Quasar outflows and the formation of dwarf galaxies. Monthly Notices of the Royal Astronomical Society, 298, 577, doi: 10.1046/j.1365-8711.1998.01703.x
[14.] Pachankis, Y. (2021a).The Weak and Strong Forces in Observational Astronomy from Small Magellanic Cloud, Tech. rep. https: //www.academia.edu/video/l48z5l
[15.] Pachankis, Y. (2022).A Multi-wavelength Data Analysis with Multi-mission Space Telescopes. International Journal of Innovative Science and Research Technology, Volume 7, Issue 1, January - 2022.PP: 701-708. doi: 10.5281/zenodo.6044904
[16.] Pachankis, Yang I. (2021b). Research on the Kerr-Newman Black Hole in M82 Confirms Black Hole and White Hole Juxtapose, Academia Letters. Doi: 10.20935/AL3199
[17.] Pence, W. D., Chiappetti, L., Page, C. G., Shaw, R. A., &Stobie, E. (2010). A&A, 524, A42, doi: 10.1051/0004-6361/201015362
[18.] Penrose, R. (1965). Gravitational Collapse and Space-Time Singularities. Phys. Rev. Lett., 14, 57, doi: 10.1103/PhysRevLett.14.57
[19.] Traver, Tiffani(2014). Trigonometry in the Hyperbolic Plane.
[20.] Weinberg, S. (1957). Role of Strong Interactions in Decay Processes. Phys. Rev., 106, 1301, doi: 10.1103/PhysRev.106.1301